Isaacson & Johnson (1975). Very recently, a level close to the single-atom identification has been demonstrated (Mory & Colliex, 1989). A major obstacle is then often radiation damage, and consequent specimen modification induced by the very intense primary dose required for obtaining sufficient SNR values.

On the other hand, the EELS technique has long been less fruitful for investigating low concentrations of impurities within a matrix. This is a consequence of the very high intrinsic background under the edges of interest: in most applications, the atomic concentration detection limit was in the range 10^{-3} to 10^{-2}. The introduction of satisfactory methods for processing the systematic sources of noise in spectra acquired with parallel detection devices (Shuman & Kruit, 1985) has greatly modified this situation. One can now take full benefit from the very high number of counts thus recorded within a reasonable time (10^6 to 10^7 counts per channel) and detection of calcium of the order of 10^{-5} atomic concentration in an organic matrix has been demonstrated by Shuman & Somlyo (1987).

(*c*) *Crystallographic information in EELS*

Although not particularly suited to solving crystal-structure problems, EELS carries structural information at different levels:

In a crystalline specimen, one detects orientation effects on the intensity of core-loss edges. This is a consequence of the channelling of the Bloch standing waves as a function of the crystal orientation This observation requires well collimated angular conditions and inelastic localization better than the lattice spacing responsible for elastic diffraction. When these criteria apply, the changes in core-loss excitations with crystallographic orientation can be used to determine the crystallographic site of specific atoms (Tafto & Krivanek, 1982). An equivalent method, known as ALCHEMI (atom location by channelling enhanced microanalysis), which involves measuring the change of X-ray production as a function of crystal orientation, has been applied to the determination of the preferential site for substitutional impurities in many crystals (Spence & Tafto, 1983).

Energy-filtered electron-diffraction patterns of core-loss edges could reveal the symmetry of the local coordination of selected atomic species rather than the symmetry of the crystal as a whole. This type of information should be compared with ELNES data (Spence, 1981).

At large scattering angles, and for energy losses far beyond the excitation threshold, the Bethe ridge [or electron Compton profile (see §§4.3.4.3.3 and 4.3.4.4.2)] constitutes a major feature easily observable in energy-filtered diffraction patterns (Reimer & Rennekamp, 1989). The width of this feature is associated with the momentum distribution of the excited electrons (Williams & Bourdillon, 1982). Quantitative analysis of the data is similar to the Fourier method for EXELFS oscillations. After subtracting the background contribution, the spectrum is converted into momentum space and Fourier transformed to obtain the reciprocal form factor $B(r)$: it is the autocorrelation of the ground-state wavefunction in a direction specified by the scattering vector $\mathbf{q}$. This technique of data analysis to study electron momentum densities is directly developed from high-energy photon-scattering experiments (Williams, Sparrow & Egerton, 1984).

4.3.4.5. *Conclusions*

Since the early work of Hillier & Baker (1944), EELS spectroscopy has established itself as a prominent technique for investigating various aspects of the electronic structure of solids, As a fundamental application, it is now possible to construct a self-consistent set of data for a substance by combination of optical or energy-loss functions over a wide spectral range (Altarelli & Smith, 1974; Shiles, Sazaki, Inokuti & Smith, 1980: Hagemann, Gudat & Kunz, 1975). Sum-rule tests provide useful guidance in selecting the best values from the available measurements. The Thomas–Reiche–Kuhn f-sum rule can be expressed in a number of equivalent forms, which all require the knowledge of a function $[\varepsilon_2, \kappa, \mathrm{Im}(-1/\varepsilon)]$ describing dissipative processes over all frequencies:

$$\left.\begin{aligned} \int_0^\infty \omega\varepsilon_2(\omega)\,\mathrm{d}\omega &= \frac{\pi}{2}\omega_p^2, \\ \int_0^\infty \omega\kappa(\omega)\,\mathrm{d}\omega &= \frac{\pi}{4}\omega_p^2, \\ \int_0^\infty \omega\left(-\frac{1}{\varepsilon(\omega)}\right)\mathrm{d}\omega &= \frac{\pi}{2}\omega_p^2. \end{aligned}\right\} \tag{4.3.4.53}$$

One defines the effective number density n_{eff} of electrons contributing to these various absorption processes at an energy $\hbar\omega$ by the partial f sums:

$$\left.\begin{aligned} n_{\mathrm{eff}}(\omega)|_{\varepsilon_2} &= \frac{m_0}{2\pi^2 e^2}\int_0^\omega \omega'\varepsilon_2(\omega')\,\mathrm{d}\omega', \\ n_{\mathrm{eff}}(\omega)|_{\kappa} &= \frac{m_0}{\pi^2 e^2}\int_0^\omega \omega'\kappa(\omega')\,\mathrm{d}\omega', \\ n_{\mathrm{eff}}(\omega)|_{-1/\varepsilon} &= \frac{m_0}{2\pi^2 e^2}\int_0^\omega \omega'\left[-\frac{1}{\varepsilon(\omega')}\right]\mathrm{d}\omega'. \end{aligned}\right\} \tag{4.3.4.54}$$

As an example, the values of $n_{\mathrm{eff}}(\omega)$ from the infrared to beyond the K-shell excitation energy for metallic aluminium are shown in Fig. 4.3.4.32. In this case, the conduction and core-electron contributions are well separated. One sees that the excitation of conduction electrons is virtually completed above the plasmon resonance only, but the different behaviour of the integrands below this value is a consequence of the fact that they describe different properties of matter: $\varepsilon_2(\omega)$ is a measure of the rate of energy dissipation from an electromagnetic wave, $\kappa(\omega)$ describes

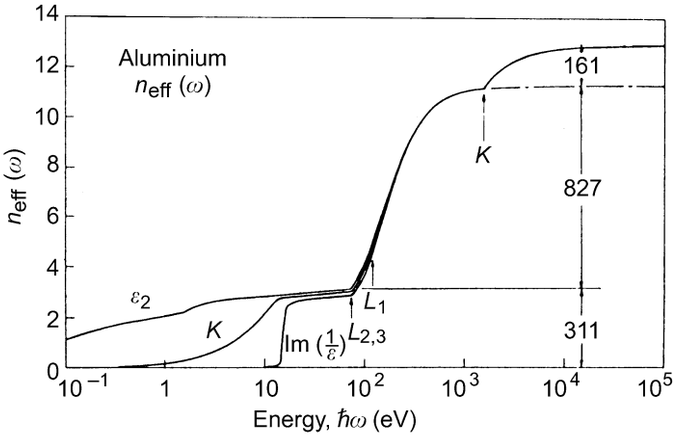

Fig. 4.3.4.32. Values of n_{eff} for metallic aluminium based on composite optical data [courtesy of Shiles *et al.* (1980)].

the decrease in amplitude of the wave, and $\mathrm{Im}[-\varepsilon^{-1}(\omega)]$ is related to the energy loss of a fast electron. The above curve shows some exchange of oscillator strength from core to valence electrons, arising from the Pauli principle, which forbids transitions to occupied states for the deeper electrons.

More practically, in the microanalytical domain, the combination of high performance attained by using EELS with parallel detection (*i.e.* energy resolution below 1 eV, spatial resolution below 1 nm, minimum concentration below 10^{-3} atom, time resolution below 10 ms) makes it a unique tool for studying local electronic properties in solid specimens.

4.3.5. Oriented texture patterns (By B. B. Zvyagin)

4.3.5.1. *Texture patterns*

The formation of textures in specimens for diffraction experiments is a natural consequence of the tendency for crystals of a highly anisotropic shape to deposit with a preferred orientation. The corresponding diffraction patterns may present some special advantages for the solution of problems of phase and structure analysis. Lamellar textures composed of crystals with the most fully developed face parallel to a plane but randomly rotated about its normal are specially important. The ease of interpretation of patterns of such textures when oriented obliquely to the primary beam (*OT* patterns) is a valuable property of the electron-diffraction method (Pinsker, 1953; Vainshtein, 1964; Zvyagin, 1967; Zvyagin, Vrublevskaya, Zhukhlistov, Sidorenko, Soboleva & Fedotov, 1979). Texture patterns (*T* patterns) are also useful in X-ray diffraction (Krinary, 1975; Mamy & Gaultier, 1976; Plançon, Rousseaux, Tchoubar, Tchoubar, Krinari & Drits, 1982).

4.3.5.2. *Lattice plane oriented perpendicular to a direction (lamellar texture)*

If in the plane of orientation (the texture basis) the crystal has a two-dimensional cell a, b, γ, the c^* axis of the reciprocal cell will be the texture axis. Reciprocal-lattice rods parallel to c^* intersect the plane normal to them (the ab plane of the direct lattice) in the positions hk of a two-dimensional net that has periods $1/a\sin\gamma$ and $1/b\sin\gamma$ with an angle $\gamma' = \pi - \gamma$ between them, whatever the direction of the c axis in the direct lattice.

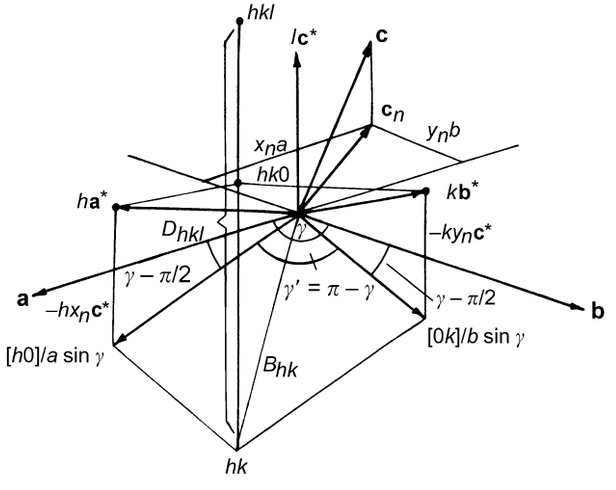

Fig. 4.3.5.1. The relative orientations of the direct and the reciprocal axes and their projections on the plane ab, with indication of the distances B_{hk} and D_{hkl} that define the positions of reflections in lamellar texture patterns.

The latter is defined by the absolute value c and the normal projection c_n on the ab plane, with components x_n, y_n along the axes a, b. In the triclinic case,

$$x_n = (c/a)(\cos\beta - \cos\alpha\cos\gamma)/\sin^2\gamma \qquad (4.3.5.1)$$

$$y_n = (c/b)(\cos\alpha - \cos\beta\cos\gamma)/\sin^2\gamma \qquad (4.3.5.2)$$

(Zvyagin *et al.*, 1979). The lattice points of each rod with constant hk and integer l are at intervals of $c^* = 1/d_{001}$, but their real positions, described by their distances D_{hkl} from the plane ab, depend on the projections of the axes a^* and b^* on c^* (see Fig. 4.3.5.1), the equations

$$x_n = -a^*\cos\beta^*/c^* \qquad (4.3.5.3)$$

$$y_n = -b^*\cos\alpha^*/c^* \qquad (4.3.5.4)$$

being satisfied.

The reciprocal-space representation of a lamellar texture is formed by the rotation of the reciprocal lattice of a single crystal about the c^* axis. The rods hk become cylinders and the lattice points become circles lying on the cylinders. In the case of high-energy electron diffraction (HEED), the wavelength of the electrons is very short, and the Ewald sphere, of radius $1/\lambda$, is so great that it may be approximated by a plane passing through the origin of reciprocal space and normal to the incident beam. The patterns differ in their geometry, depending on the angle φ through which the specimen is tilted from perpendicularity to the primary beam. At $\varphi = 0$, the pattern consists of hk rings. When $\varphi \neq 0$ it contains a two-dimensional set of reflections hkl falling on hk ellipses formed by oblique sections of the hk cylinders. In the limiting case of $\varphi = \pi/2$, the ellipses degenerate into pairs of parallel straight lines theoretically containing the maximum numbers of reflections. The reflection positions are defined by two kinds of distances: (1) between the straight lines hk (length of the short axes of the ellipses hk):

$$B_{hk} = (1/\sin\gamma)(h^2/a^2 + k^2/b^2 - 2hk\cos\gamma/ab)^{1/2} \qquad (4.3.5.5)$$

and (2) from the reflection hkl to the line of the short axes:

$$D_{hkl} = (ha^*\cos\beta^*/c^* + kb^*\cos\alpha^*/c^* + l)c^* \qquad (4.3.5.6)$$

$$= (-hx_n - ky_n + l)/d_{001}. \qquad (4.3.5.7)$$

In patterns obtained under real conditions ($0 < \varphi < \pi/2$, accelerating voltage V proportional to λ^{-2}, distance L between the specimen and the screen), these values are presented in the scale of $L\lambda$, D_{hkl} also being proportional to $1/\sin\varphi$ with maximum value $D_{\max} = B_{hk}\tan\varphi$ for the registrable reflections. The values of B_{hk} and D_{hkl}, determined by the unit cells and the indices hkl, are the objects of the geometrical analysis of the *OT* patterns. When the symmetry is higher than triclinic, the expression for B_{hk} and D_{hkl} are much simpler.

Such *OT* patterns are very informative, because the regular two-dimensional distribution of the hkl reflections permits definite indexing, cell determination, and intensity measurements. For low-symmetry and fine-grained substances, they present unique advantages for phase identification, polytypism studies, and structure analysis.

In the X-ray study of textures, it is impossible to neglect the curvature of the Ewald sphere and the number of reflections recorded is restricted to larger d values. However, there are advantages in that thicker specimens can be used and reflections with small values of B_{hk}, especially the $00l$ reflections, can be recorded. Such patterns are obtained in usual powder cameras with the incident beam parallel to the platelets of the oriented aggregate and are recorded on photographic film in the form of hkl reflection sequences along hk lines, as was demonstrated by

references